AIP | Physics of Fluids

Large eddy simulation of longitudinal stationary vortices

Madhu Sreedhar and Saad Ragab

Citation: Physics of Fluids (1994-present) **6**, 2501 (1994); doi: 10.1063/1.868436
View online: http://dx.doi.org/10.1063/1.868436
View Table of Contents: http://scitation.aip.org/content/aip/journal/pof2/6/7?ver=pdfcov
Published by the AIP Publishing

Large eddy simulation of longitudinal stationary vortices

Madhu Sreedhar and Saad Ragab
Department of Engineering Science and Mechanics, Virginia Polytechnic Institute and State University, Blacksburg, Virginia 24061

(Received 27 October 1993; accepted 23 March 1994)

The response of longitudinal stationary vortices when subjected to random perturbations is investigated using temporal large-eddy simulation. Simulations are obtained for high Reynolds numbers and at a low subsonic Mach number. The subgrid-scale stress tensor is modeled using the dynamic eddy-viscosity model. The generation of large-scale structures due to centrifugal instability and their subsequent breakdown to turbulence is studied. The following events are observed. Initially, ring-shaped structures appear around the vortex core. These structures are counter-rotating vortices similar to the donut-shaped structures observed in a Taylor–Couette flow between rotating cylinders. These structures subsequently interact with the vortex core resulting in a rapid decay of the vortex. The turbulent kinetic energy increases rapidly until saturation, and then a period of slow decay prevails. During the period of maximum turbulent kinetic energy, the normalized mean circulation profile exhibits a logarithmic region, in agreement with the universal inner profile of Hoffman and Joubert [J. Fluid Mech. **16**, 395 (1963)].

I. INTRODUCTION

Large-scale vortices occur in technology, and in nature very often. In the laboratory, these vortices are either artificially generated or freely formed as a result of certain aerodynamic processes. Wakes of lifting bodies contain vortex sheets of high streamwise vorticity. The sheets usually roll up and form strong streamwise vortices. The trailing vortices of large aircraft on the runway pose a serious threat to following smaller aircrafts. Such powerful vortices are also shed from a submarine during a rapid maneuver, which can lead to undesirable pressure forces, and they tend to persist in the far wake.

Artificial vortices are generated for a variety of reasons. In combustion chambers, they are used to enhance the mixing. In mixing layers, streamwise vortices develop in the braid region causing large-scale instabilities and accelerate the breakdown to turbulence. Trapped vortices on a delta wing surface contribute substantially to the lift. In these vortices, axial velocities may or may not be strong. In most cases, these vortices tend to be turbulent or they are created in a turbulent environment.

Instabilities in vortices are due to a variety of mechanisms. In trailing vortices where circulation is a monotone function of radius, the presence of axial velocity serves as a major source of instability. In vortices without mean axial velocity component, Rayleigh[1] showed that centrifugal instability can cause disturbances to grow if the mean circulation profile decreases with the radius. The emphasis of this work is to investigate the transition and turbulent behavior of vortices as a result of the centrifugal instability. The turbulence created and its subsequent fate is investigated.

A. Large eddy simulation

Turbulent flows consist of a wide range of temporal and spatial scales of motions. Direct numerical simulations (DNS) resolve all the scales, but are limited to low Reynolds numbers due to the wide disparity of scales at high Reynolds numbers. In the Reynolds-averaged Navier–Stokes (RANS) approach, the mean flow quantities are computed, while the rest of the flow field is modeled.

In large-eddy simulations (LES) the large-scale motions in a turbulent flow field are resolved. They contain most of the turbulent kinetic energy. Typically, these scales are imposed upon the flow field by the external boundaries or the geometry of immersed bodies. Turbulence modeling is required for the smaller scale eddies, which are independent of the flow geometry, and hence more universal. Such a model is expected to be less complicated than the models required for RANS, where the model accounts for all the scales other than the mean flow.

An important ingredient of LES is the subgrid-scale (SGS) model. A new subgrid-scale eddy-viscosity model has been developed by Germano *et al.*[2] In this model, the model constants are computed dynamically as the simulation progresses rather than input *a priori*. It performs very well in transitional flow and near wall regions. It has been extended to compressible flows by Moin *et al.*[3] Several modifications have been proposed to the model by Lilly[4] and Wong.[5] This model is widely gaining popularity and needs to be tested for complex flows. The present work uses this model.

B. Turbulent vortex flows

Three-dimensional flow separation and the ensuing vortical motions occur in many aerodynamic applications. The fate of these vortices depend on a variety of factors. The turbulence that gets engulfed into the vortex during its formation and that present in the surroundings affects the dynamics of these vortices. The structure and decay of turbulence in these vortices is an area that demands further investigation. The turbulence can cause rapid diffusion of the angular momentum of the vortex on one hand, while the rotating mean flow field can cause a slow decay of the turbulence.

Lamb[6] considered the laminar diffusion of a line vortex in time. The diffusion of a vortex in turbulent flow was stud-

1070-6631/94/6(7)/2501/14/$6.00

ied by Squire.[7] He conjectured that eddy viscosity for this type of flow may be taken to be proportional to the circulation around the vortex, and the solution is then similar to the solution for the decay of a vortex in laminar flow. Newman[8] found that the assumption of the constant eddy viscosity, as proposed by Squire, did not compare well with the experiments. Dosanjh *et al.*[9] found that for turbulent vortices the decay rates of velocity and other geometrical parameters were eight to ten times faster than what is given by molecular kinematic viscosity. Owen[10] found that the turbulent viscosity depends on the Reynolds number, defined with respect to the circulation and not on the initial circulation, as Squire proposed. Hoffman and Joubert[11] put forward a triple-layer structure: A viscous core, an inner layer where the circulation has a logarithmic distribution, and an outer layer. They also found that the vortices were completely independent of viscous effects above a certain Reynolds number. Nielsen and Schwind[12] presented a theory for the different stages in the evolution of trailing vortices. The three-layered structure is compared to a turbulent boundary layer, which also possesses a similar structure.

Govindaraju and Saffman[13] argue that for a vortex to grow at a rate greater than that due to molecular diffusion alone, an overshoot in the radial distribution of circulation is required. This overshoot implies a region of negative slope in the square of circulation. This is consistent with the Rayleigh criterion.[1] Uberoi[14] also points out that turbulence in a vortex can be generated and maintained only if the circulation has a nonmonotone variation. Uberoi calls vortices with nonmonotone variation swirls. He concludes that a vortex is stable while a combination of a vortex and a swirl is unstable. This nonuniform variation of circulation leads to the argument that a vortex has a multilayered structure.

Saffman[15] considers a triple-layer structure similar to that of Hoffman and Joubert.[11] He puts forward a theory to show the dependence of the decay of a trailing line vortex on Reynolds number. Phillips[16] also puts forward a three-layered structure for a trailing vortex during rollup. He found a dependency of circulation and Reynolds stresses on the initial spanwise distribution of circulation on the wing. He also discusses the apparent dependence of trailing vortices on the Reynolds number.

There has been quite a few experimental studies in the literature on turbulence decay and vortex wakes other than the ones mentioned above. Newman[8] reported the earliest measurements in a turbulent vortex. McCormick *et al.*[17] made detailed velocity measurements during an actual flight test. Chigier and Corsiglia[18] made wind tunnel measurements of wing wake turbulence. They reported that the axial velocity changes from a wake-like to a jet-like profile, as the angle of attack is increased. Corsigilia *et al.*[19] measured the velocity profiles of wing tip vortices over a rectangular wing, and found that the tangential velocity distributions had the same functional form as determined by Hoffman and Joubert.[11]

The decay rates of the maximum tangential velocity of the vortices from different experiments showed substantial scatter. Lezius[20] explained this scatter as the result of a time varying eddy viscosity due to the nonequilibrium nature of the turbulent flow field in the vortex. His arguments are as follows. The mechanics of turbulent decay depends on the levels of turbulence intensities that are introduced into the vortex during its formation. For example, the turbulence in a boundary layer that is convected into the wake can get engulfed into the vortex during the rollup. This can interact with the mean shearing motion within the vortex to produce more turbulence. Lezius also concluded that this can create an imbalance between the initial turbulence levels and those that can be maintained by the vortex, and that creates a nonequilibrium condition. This leads to an eddy viscosity that varies with time. We note here that this is an ideal situation for the use of the dynamic eddy-viscosity model of Germano *et al.*[2] Lezius also points out that under equilibrium conditions the decay rates approach the $t^{-1/2}$ law. Sarpkaya and Suthon[21,22] and Sarpkaya[23] describe the three-dimensional structures due to the interaction of turbulent and laminar vortices with deformable free surfaces. They describe in detail the formation of scars, striations, and whirls among other observable three-dimensional structures. Dommermuth and Yue[24] and Dommermuth[25] performed numerical simulations of vortex tubes impinging on free surfaces and slip/no-slip walls. They also observed striations similar to the ones mentioned by Sarpkaya and Suthon.[21,22] According to Sarpkaya and Suthon,[21,22] the presence of striations is due to subsurface instabilities that can manifest, even in the absence of free surfaces. Another feature worth mentioning here is the presence of U-shaped vortices that wrap around the vortex core. Donaldson and Sullivan[26] also mention the experimental observations of ring-shaped structures encircling the vortex core when there is an overshoot in the circulation.

Measurements of the Reynolds stress tensor and other turbulent quantities of a turbulent trailing vortex were done by Poppleton.[27] His flow field consisted of jets superimposed on a vortex generated by a differential airfoil. Singh[28] also measured some components of the Reynolds stress tensor for a vortex from a highly loaded single airfoil. A recent source of Reynolds-stress measurements in a turbulent trailing vortex is Phillips and Graham.[29] Their measurements are for a wide range of axial flows. The instantaneous velocity distribution in trailing vortices generated by lifting hydrofoils has been measured by Green and Acosta.[30] They found rapid peak to peak fluctuations of axial velocity along the centerline of the vortex.

Turbulence modeling for swirling flows is a difficult problem. Granger[31] presented a review of the existing models and their applications to turbulent vortices. Lilley[32] considered various models and suggested that a nonisotropic model is found to show more realistically the effects of swirl on a jet-like flow. Donaldson and Sullivan,[26] using their invariant modeling technique, solved for the Reynolds stresses for the decay of an isolated vortex. Baldwin[33] used a formula for the eddy-viscosity coefficient that depends on the turbulent energy of the flow field. Bilanin *et al.*[34] simulated the dissipation of turbulent vortices in a simplified neutral atmosphere. They used a second-order closure model to study the effect of background turbulence, wind shear, and the proximity to the ground on the rate of decay of vortex wakes. It was found that the decay rate increased with increasing background turbulence. Zheng and Ash[35] compared the Reynolds stress transport model with zero-equation, one-equation, and two-equation eddy-viscosity models. They found that all the eddy-viscosity models showed excessive dissipation. A similar result was found earlier by Hogg and Leschziner[36] for confined flows. They used a finite volume formulation for comparing the performance of a two-equation eddy-viscosity model to a Reynolds stress transport closure model for highly swirling confined flow. Some of the recent developments in the turbulence modeling of swirling flows can also be found in Sloan *et al.*,[37] Khodadadi and Vlachos,[38] Nikjooy and Mongia,[39] and Chang and Chen.[40]

Since large-scale instabilities and structures play a vital role in the evolution of turbulent vortices, it is essential that we resolve all the large-scale motions accurately. Large-eddy simulation can be used very effectively to address these issues and relax the stringent requirement on turbulence models required for RANS. The majority of the large-eddy simulations to date use the eddy-viscosity model of Smagorinsky.[41] Bardina *et al.*[42] used the Smagorinsky model for studying the effect of rotation on isotropic turbulence. The main drawback of the Smagorinsky model is that the model constant has to specified *a priori*. The dynamic model of Germano *et al.*[2] has the flexibility of being able to change temporally and spatially, depending on the turbulence field. So it can adjust itself to the different layers of the turbulent vortex, in addition to evolving in time. Squire[43] recently applied the dynamic model to rotating isotropic turbulence and compared with DNS data. At higher rotation rates it was found that the SGS dissipation reduced considerably. The dynamic model alone did not provide enough dissipation, but the inclusion of molecular viscosity into the calculation enabled good comparison with the DNS results.

Even though the linear stability analysis has been successfully used to understand the stability of vortices, further techniques are required to understand the nonlinear interaction of various modes. The growth of the instability modes results in the formation of large-scale structures, which will then control the dynamics of the flow field. There is a need to understand these mechanisms and identify the large-scale structures and their subsequent development.

C. Objectives

The main objectives of this work can be summarized as follows: (i) Study the response of longitudinal vortices to random perturbations using LES. The dynamic model is applied to account for the subgrid stresses. (ii) Identify the large-scale structures that are created due to centrifugal instabilities. (iii) Follow the evolution of mean-flow quantities and modal energies. Compare these quantities with the available experimental profiles and linear stability results.

II. EQUATIONS OF LARGE-EDDY SIMULATION

The Navier–Stokes equations are Favre filtered. Let an overtilde denote a Favre-filtered quantity and an overbar denote the space filtering operation. Following Erlebacher *et al.*,[44] we introduce the Favre-filtered field,

$$\tilde{f}=\frac{\overline{\rho f}}{\bar{\rho}} \tag{1}$$

and decompose the total flow field into a resolvable field $\tilde{f}$ and a subgrid-scale field f',

$$f=\tilde{f}+f'. \tag{2}$$

Filtering the mass and momentum equations, we obtain

$$\frac{\partial\bar{\rho}}{\partial t}+\frac{\partial(\bar{\rho}\tilde{u}_j)}{\partial x_j}=0, \tag{3}$$

$$\frac{\partial\bar{\rho}\ \tilde{u}_i}{\partial t}+\frac{\partial}{\partial x_j}[\bar{\rho}\tilde{u}_i\tilde{u}_j+\bar{p}\,\delta_{ij}+R_{ij}-\bar{\tau}_{ji}]=0, \tag{4}$$

where

$$R_{ij}=\bar{\rho}(\widetilde{u_i u_j}-\tilde{u}_i\tilde{u}_j) \tag{5}$$

is the subgrid-stress tensor and $\bar{\tau}_{ij}$ is the viscous stress tensor. The filtered pressure is given by

$$\bar{p}=\bar{\rho}R\tilde{T}, \tag{6}$$

where $\tilde{T}$ is the resolvable temperature field and R is the gas constant.

Filtering the total energy equation, we obtain

$$\frac{\partial(\bar{\rho}\tilde{E}+k)}{\partial t}+\frac{\partial}{\partial x_j}[(\bar{\rho}\tilde{E}+\bar{p})\tilde{u}_j+K_j+Q_j-\overline{u_i\tau_{ji}}+\overline{q_j}]=0, \tag{7}$$

where

$$\tilde{E}=\tilde{e}+\tfrac{1}{2}\tilde{u}_i\tilde{u}_i, \tag{8}$$

$$Q_j=C_p\bar{\rho}(\widetilde{Tu_j}-\tilde{T}\tilde{u}_j), \tag{9}$$

$$k=\tfrac{1}{2}(R_{ii}), \tag{10}$$

and

$$K_j=\tfrac{1}{2}\bar{\rho}(\widetilde{\tilde{u}_i\tilde{u}_i\tilde{u}_j}-\tilde{u}_i\tilde{u}_i\tilde{u}_j). \tag{11}$$

A. A subgrid-scale model

The subgrid-stress term is modeled by an eddy-viscosity model. An eddy-viscosity model typically contains a characteristic length scale and a time scale (or a velocity scale). In LES, the filter width is usually chosen as the length scale. In the Smagorinsky model, the time scale is an invariant of the strain rate tensor of the resolvable velocity field. The generalization of the Smagorinsky formula to compressible flows is due to Erlebacher *et al.*,[44] and is given by

$$R_{ij}=-2C_R\,\Delta^2\bar{\rho}\sqrt{\tilde{\Pi}}(\widetilde{S_{ij}}-\tfrac{1}{3}\widetilde{S_{kk}}\delta_{ij})+\tfrac{2}{3}C_I\,\Delta^2\bar{\rho}\ \tilde{\Pi}\delta_{ij}, \tag{12}$$

where

$$\widetilde{S_{ij}}=\frac{1}{2}\left(\frac{\partial\tilde{u}_i}{\partial x_j}+\frac{\partial\tilde{u}_j}{\partial x_i}\right) \tag{13}$$

is the rate of strain tensor of the resolvable field, and

$$\tilde{\Pi}=\widetilde{S_{ij}}\widetilde{S_{ij}}. \tag{14}$$

In Eq. (12), Δ is the filter width and C_R and C_I are the model constants.

The temperature–velocity correlation terms are modeled by a gradient-transport model:

$$Q_j=-C_p\bar{\rho}C_T\Delta^2\sqrt{\tilde{\Pi}}\,\frac{\partial\tilde{T}}{\partial x_j}, \tag{15}$$

where the constant C_T is written as

$$C_T=\frac{C_R}{\mathrm{Pr}_T}. \tag{16}$$

Here Pr_T is a turbulent Prandtl number.

Following Ragab *et al.*,[45] the term K_j is approximated as the rate of work done by the SGS stresses,

$$K_j=R_{ij}\tilde{u}_i, \tag{17}$$

where R_{ij} is given by Eq. (12).

The parameter Δ^2 is mesh dependent, and in this work is defined by $\Delta^2=[(\Delta x)^2+(\Delta y)^2+(\Delta z)^2]/3$. The numerical values of C_R and C_I depend on how Δ^2 is defined. These constants are not universally defined and depend on individual applications. In the work of Erlebacher *et al.*,[44] Δ^2 is defined by $4\delta^2$, where δ is the mesh size. They found that C_R and C_I to be 0.012 and 0.0066, respectively, for homogeneous isotropic turbulence. These values were obtained by *a priori* comparison of the model with the DNS data. For the turbulent Prandtl number Pr_T, they obtained a value of 0.5. Zang *et al.*[46] showed that C_I may not be very important for low turbulent Mach numbers, and may be neglected. They also used the conventional value of 0.7 for the turbulent Prandtl number Pr_T.

In the present investigation, since the computations are for low subsonic Mach numbers, C_I was neglected. For the turbulent Prandtl number Pr_T, the conventional value of 0.7 was used. But C_R was not specified *a priori*; it was obtained using the dynamic modeling procedure of Germano *et al.*,[2] as described in Secs. II B and II C.

B. A dynamic SGS model

This model provides an elegant way for computing the model constant C_R. This eliminates the need for tuning the model constant for different flow situations or different regions of the same flow field. When the flow is laminar in certain sections of the flow field, this model turns itself off locally. This feature is very essential for transitional flows and wall-bounded flows, where viscous stresses dominate near the wall. This model was first proposed by Germano *et al.*,[2] and since then it has been gaining acceptance. It has been used for transitional supersonic flow over a flat plate by El Hady *et al.*[47] Model predictions were found to be very satisfactory. Liu and Piomelli[48] applied it to study the interaction of embedded vortices with a spatially developing boundary layer. Akselvoll and Moin[49] compared the results of the dynamic model with DNS for a backward facing step. They obtained very good comparison. To the best of our knowledge, the only application of dynamic model to rotating turbulence reported to date is the work of Squire.[43]

The key feature of the dynamic model is the application of a test filter, which has a filter width larger than the resolvable field filter. This results in a field that has scales larger than the resolvable field. The spectral information contained within these two fields is utilized to compute the values of the model constants. The test-filter width will be denoted by $\hat{\Delta}$ and a test-filtered quantity will be denoted by $\hat{u}$. If a grid resolved quantity is filtered again with the test filter, it will be denoted as $\hat{\tilde{u}}$. The following derivation follows Moin *et al.*[3] with the modifications proposed by Lilly.[4] In the momentum equation, we need to model the SGS stress term,

$$R_{ij}=\bar{\rho}(\widetilde{u_iu_j}-\tilde{u}_i\tilde{u}_j). \tag{18}$$

Using (1), this can be rewritten as

$$R_{ij}=\overline{\rho u_iu_j}-\frac{\overline{\rho u_i}\,\overline{\rho u_j}}{\bar{\rho}}, \tag{19}$$

and the model for R_{ij} is given by Eq. (12).

The test-filtered stresses $\mathbf{R}_{ij}$ and their model are defined by direct analogy to the equations for the SGS stresses R_{ij}. They are

$$\mathbf{R}_{ij}=\widehat{\overline{\rho u_iu_j}}-\frac{\widehat{\overline{\rho u_i}}\cdot\widehat{\overline{\rho u_j}}}{\hat{\bar{\rho}}} \tag{20}$$

and

$$\mathbf{R}_{ij}=-2C_R\,\hat{\Delta}^2\hat{\bar{\rho}}\sqrt{\hat{\tilde{\Pi}}}(\widehat{\tilde{S}_{ij}}-\tfrac{1}{3}\widehat{\tilde{S}_{kk}}\delta_{ij})+\tfrac{2}{3}C_I\hat{\Delta}^2\hat{\bar{\rho}}\;\hat{\tilde{\Pi}}\delta_{ij}. \tag{21}$$

Applying the test filter to (19), and then subtracting the result from (20), we obtain

$$L_{ij}\equiv\mathbf{R}_{ij}-\hat{R}_{ij}, \tag{22}$$

where

$$L_{ij}=\widehat{\bar{\rho}\tilde{u}_i\tilde{u}_j}-\frac{\widehat{\bar{\rho}\tilde{u}_i}\widehat{\bar{\rho}\tilde{u}_j}}{\hat{\bar{\rho}}}. \tag{23}$$

The term L_{ij} is referred to as the Leonard term, and is fully computable from the resolved variables.

For obtaining C_R, the trace-free SGS stress terms are considered. Thus,

$$R_{ij}-\tfrac{1}{3}R_{kk}\delta_{ij}=-2C_R\,\Delta^2\bar{\rho}\sqrt{\tilde{\Pi}}(\widetilde{S_{ij}}-\tfrac{1}{3}\widetilde{S_{kk}}\delta_{ij}). \tag{24}$$

The corresponding test-filtered stresses are

$$\mathbf{R}_{ij}-\tfrac{1}{3}\mathbf{R}_{kk}\delta_{ij}=-2C_R\,\hat{\Delta}^2\hat{\bar{\rho}}\sqrt{\hat{\tilde{\Pi}}}(\widehat{\tilde{S}_{ij}}-\tfrac{1}{3}\widehat{\tilde{S}_{kk}}\delta_{ij}). \tag{25}$$

Combining (22), (23), (24), and (25) yields

$$\begin{aligned}&\widehat{\bar{\rho}\tilde{u}_i\tilde{u}_j}-\frac{1}{\hat{\bar{\rho}}}\,\widehat{\bar{\rho}\tilde{u}_i\tilde{u}_j}-\frac{1}{3}\,(\widehat{R_{kk}}-\mathbf{R}_{kk})\,\delta_{ij}\\ &\quad=2C_R\,\Delta^2\bar{\rho}\sqrt{\tilde{\Pi}}\left(\widetilde{S_{ij}}-\frac{1}{3}\,\widetilde{S_{kk}}\delta_{ij}\right)\\ &\qquad-2C_R\,\hat{\Delta}^2\hat{\bar{\rho}}\sqrt{\hat{\tilde{\Pi}}}\left(\widehat{\tilde{S}_{ij}}-\frac{1}{3}\,\widehat{\tilde{S}_{kk}}\delta_{ij}\right).\end{aligned} \tag{26}$$

This is rewritten as

$$N_{ij}=C_RM_{ij}, \tag{27}$$

where the definitions of N_{ij} and M_{ij} follows directly from the Eq. (26). This represents five equations to be solved for one unknown C_R. Following Lilly,[4] a least-squares approach is utilized to compute C_R.

An averaging procedure is usually adopted to make these constants well conditioned. These averages are generally taken along a direction in which the turbulence is assumed to be homogeneous. The constants thus obtained are independent of the directions in which turbulence is homogeneous. Therefore, after averaging C_R becomes

$$C_R=\frac{[N_{ij}M_{ij}]}{[M_{ij}M_{ij}]}, \tag{28}$$

where $[\cdots]$ indicates an averaged quantity. There are some mathematical inconsistencies associated with treating C_R as a constant in the filtering operation indicated in the first term of the RHS of Eq. (26), and with the averaging process. Akselvoll and Moin[49] rectified these inconsistencies in their dynamic localization technique, and found that the inconsistencies due to the averaging process have only minimal effects on the results for the flow over a backward facing step.

C. Filtering

For the application of a dynamic model, a test filter needs to be defined. This filter has a filter width larger than the resolvable field filter. Most commonly used filters are the sharp cutoff filter in the Fourier space and the box filter in the physical space.

In a sharp cutoff filter, all the Fourier modes having wave numbers greater than the specified cutoff, $k_c=\pi/\Delta_f$, are removed. This filter is suitable when there are two or more homogeneous directions in the calculations along which periodic boundary conditions are used. The sharp cutoff filter has been used for a variety of flow fields (El-Hady *et al.*,[47] Liu and Piomelli,[48] and Moin *et al.*[3]).

A box filter is defined in physical space. This represents a uniformly weighted averaging over a finite volume in space. This filter is used with finite-difference schemes with nonperiodic boundary conditions. In calculations involving nonuniform grids, this type of filter is generally used. See Akselvoll and Moin[49] and Zang *et al.*[50]

In the present temporal investigation, the turbulence is assumed to be homogeneous only in the axial direction. However, a box filter is used in all three directions. The averaging is done in the homogeneous direction only. The model constant C_R is computed as a function of the other two spatial directions and time. More details of the application of the box filter can be found in Sreedhar.[51]

D. Finite-difference methods

The numerical scheme used in this investigation is a modified MacCormack scheme developed by Gottlieb and Turkel.[52] This scheme is fourth order in space for the convective terms and second order for the diffusion terms and time. Details of the method can be found in Ragab *et al.*[45]

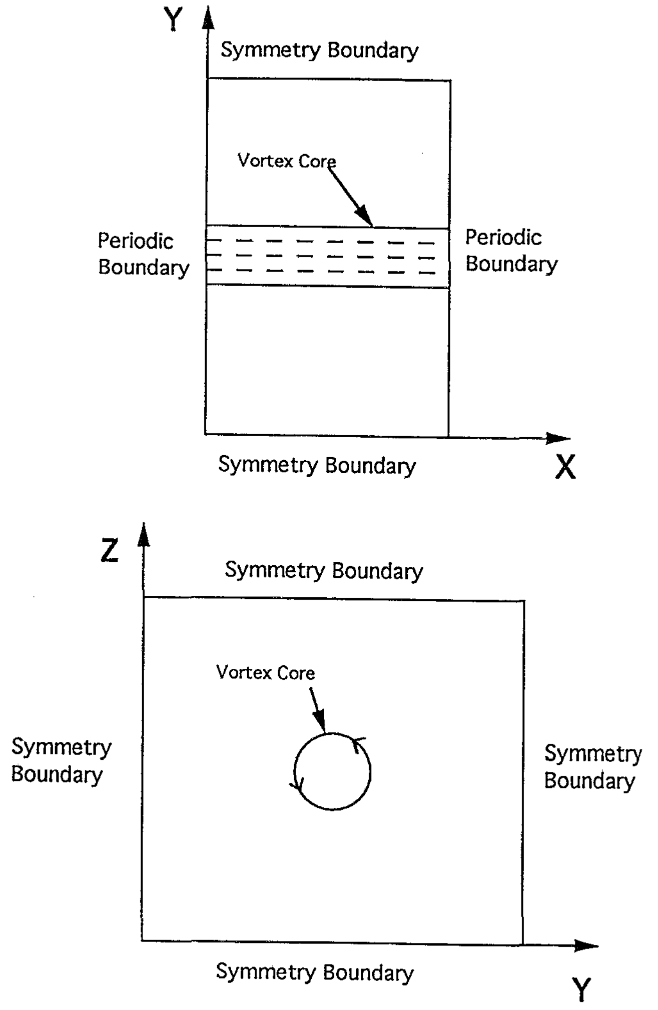

FIG. 1. Computational domain and boundary conditions. The vortex core is exaggerated.

III. RESULTS AND DISCUSSION

The large-scale structures developing due to centrifugal instabilities in stationary vortices are studied. Temporal simulation is performed so that adequate grid resolution can be obtained. The simulations are for a low subsonic Mach number of 0.2 based on maximum tangential velocity and the far-field speed of sound, which should make the calculations very near the incompressible limit.

A. Initial and boundary conditions

The reference length δ_0 is the initial core radius. The core radius is the radius, where the tangential velocity is maximum. The reference velocity V_0 is the maximum initial tangential velocity. The Reynolds number $V_0\delta_0/\nu$ is 100 000. Periodic boundary conditions are imposed along the axis of the vortex. Symmetry boundary conditions are used in the other two directions in the cross plane; see Fig. 1. The application of symmetry conditions in the cross-plane implies the presence of an infinite number of image vortices in both directions, and the attention is focused on one such vortex. Since we are using a large domain in the cross-plane in com-

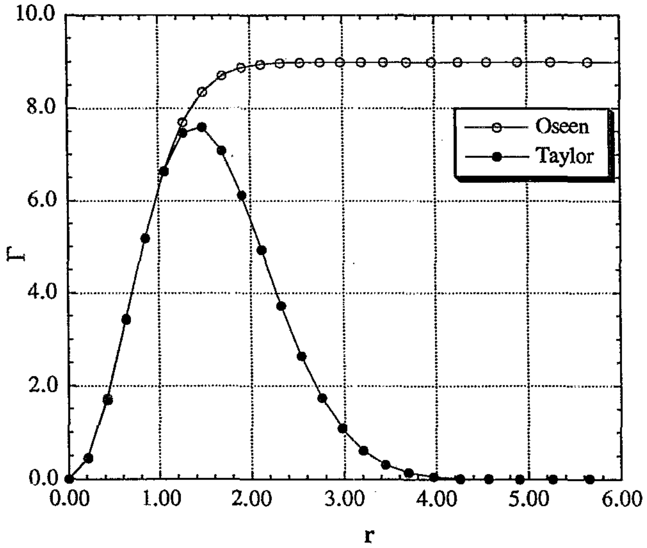

FIG. 2. Radial variation of the circulation for the Taylor vortex and the Oseen vortex. Since the Taylor vortex has a nonmonotone variation of circulation it is unstable to inviscid axisymmetric disturbances.

parison with the vortex core, it is our belief that this should have only minimal effects on the large-scale structures and the turbulence created due to centrifugal instability.

The initial field consists of the mean tangential velocity profile of a Taylor vortex or a Lamb–Oseen vortex, hereafter called an Oseen vortex, with superimposed random perturbations.

The tangential velocity profile of the Taylor vortex is

$$U_\theta = C_1 r e^{-C_2 r^2},$$

and that of the Oseen vortex is

$$U_\theta = (C_3/r)(1 - e^{-C_4 r^2}),$$

where $C_1 = e^{(1/2)}$, $C_2 = \frac{1}{2}$, $C_3 = 1.398$, and $C_4 = 1.2564$. These values are chosen so that the maximum tangential velocity occurs at unit radius. The initial mean axial and radial velocities are both zero. The Taylor and Oseen vortices are exact solutions to the unsteady incompressible Navier–Stokes equations in cylindrical coordinates (Panton[53]). The mean pressure is obtained by integrating the radial momentum equation,

$$\frac{\partial p}{\partial r} = \frac{\rho U_\theta^2}{r}.$$

The radial distribution of circulation is shown in Fig. 2. According to the Rayleigh centrifugal instability criterion, the Taylor vortex is unstable to inviscid axisymmetric disturbances due to the nonmonotone variation of circulation, whereas the Oseen vortex is stable.

B. Computational domain

The computational domain extends from $-14\delta_0$ to $+14\delta_0$ in the two directions in the cross-plane (YZ) for the Taylor vortex, while it extends from $-30\delta_0$ to $+30\delta_0$ for the Oseen vortex. The reason for using a larger domain for the Oseen vortex is due to the slow radial decay of the velocity profile. In the homogeneous axial direction (X), the domain is chosen to be $2\pi\delta_0$.

A total of $N_x = 64$ points is used in the axial direction, while $N_y = N_z = 96$ points are used in the cross-plane. The grid is stretched in the cross-plane so that near the vortex core a fine grid resolution is obtained. The vortex core is described with 18 points inside the core diameter.

For computing the mean flow profiles and the modal energies, the simulated data, which is in Cartesian coordinates (x,y,z), is transformed to cylindrical coordinates (x,r,θ), using a sixth-order Lagrange interpolation formula.

C. Comparison with linear stability

For comparison with linear stability analysis, a disturbance field of the normal mode form is superimposed on the mean vortex profile. The normal mode form is

$$u' = A(r) e^{i(\alpha x - n\theta - \omega t)} + \text{c.c.},$$

where α is the wave number in the axial direction, n is the mode number in the azimuthal direction, and ω is the complex frequency. Depending on the sign of the growth rate ω_i, the amplitude of the disturbance will grow or decay with time.

An unstable mode of the Taylor vortex is superimposed on the mean profiles. The (1,0) mode is chosen. The initial maximum amplitude of the radial velocity component is two percent of the maximum mean tangential velocity. The local growth rate of that mode after one time step is then compared with the exact growth rate. The local growth rate of a Fourier mode (m,n) is computed by performing a Fourier analysis in the axial and the azimuthal directions. The resulting Fourier coefficients are functions of the radial direction r and the local kinetic energy e_{mn} is

$$e_{mn}(r,t) = \tfrac{1}{2}(\hat{u}\hat{u}^* + \hat{v}\hat{v}^* + \hat{w}\hat{w}^*)_{mn},$$

where m and n are, respectively, the mode numbers in the axial and azimuthal directions. The local kinetic energy of a particular mode (m,n) is compared with the initial value of that mode to obtain the local growth rate. According to the linear stability theory, the growth rate is independent of r. However, because of the nonuniformity of the truncation and interpolation errors, the numerical simulations predict a growth rate that may depend on r.

The Oseen vortex is stable to linear disturbances. For comparison with linear stability, another component of mean velocity is added to make the vortex unstable. So a mean axial velocity component is superimposed on the tangential velocity profile of the Oseen vortex.

The resulting vortex is actually the q vortex (Lessen *et al.*[54]). This vortex has many growing modes according to the linear theory. The (1,1) mode was superimposed on the mean profiles. The initial maximum amplitude of the radial velocity disturbance is two percent of the maximum mean tangential velocity. Figure 3 shows the error in the local growth rate of the (1,0) mode for the Taylor vortex and the (1,1) mode for the q vortex after one time step, in comparison with the linear stability. The error is less than two percent in both the cases.

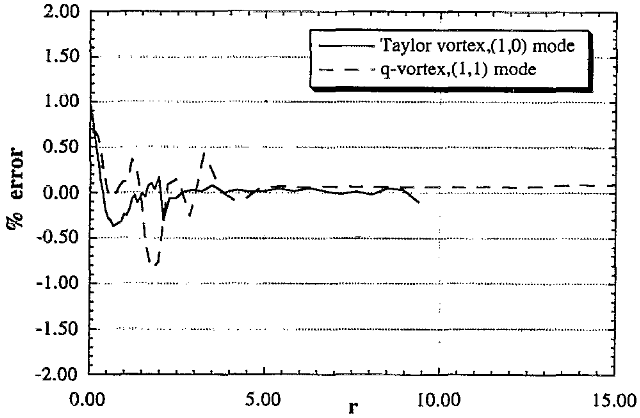

FIG. 3. The error in the local growth rate in comparison with the linear stability for the Taylor vortex and the q vortex. The flow was initialized with the basic state and the (1,0) mode for the Taylor vortex and the basic state and the (1,1) mode for the q vortex.

The previous local growth rate comparisons are shown after one time step. For long time comparison, an integrated modal energy is computed and compared with linear stability predictions. The integrated modal energy of a Fourier mode (m,n) is obtained by integrating $e_{mn}(r,t)$ in the radial direction. Thus the integrated modal energy E_{mn} is given by

$$E_{mn}(t)=\frac{1}{2}\int_0^{r_{\max}}(\hat{u}\hat{u}^*+\hat{v}\hat{v}^*+\hat{w}\hat{w}^*)_{mn}\,dr.$$

Figure 4 shows the percentage error in the growth of the integrated modal energy of the (1,1) mode, in comparison with the linear stability predicted growth rate. The maximum error is less than two percent after 200 time steps. The good agreement between the theory and numerical computation indicated in Figs. 3 and 4 is a check for the correctness of the code.

D. Large-scale structures

A random disturbance is superimposed on the mean profiles, so that no particular mode or structure is biased in the numerical simulation. The RMS value of the random disturbance is two percent of the maximum mean tangential velocity. The random disturbance is multiplied by a function that exponentially decays away from the vortex core. The simulation is done for a nondimensional time of about 52. In terms of the initial core radius and the maximum tangential velocity, this is the time taken by a particle at the initial core radius to encircle the core approximately eight times.

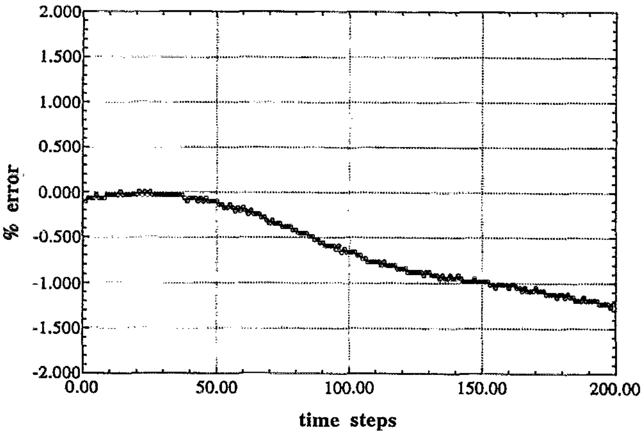

FIG. 4. Percentage error in modal energy growth rate after 200 time steps. The flow was initialized with the q vortex and the (1,1) mode.

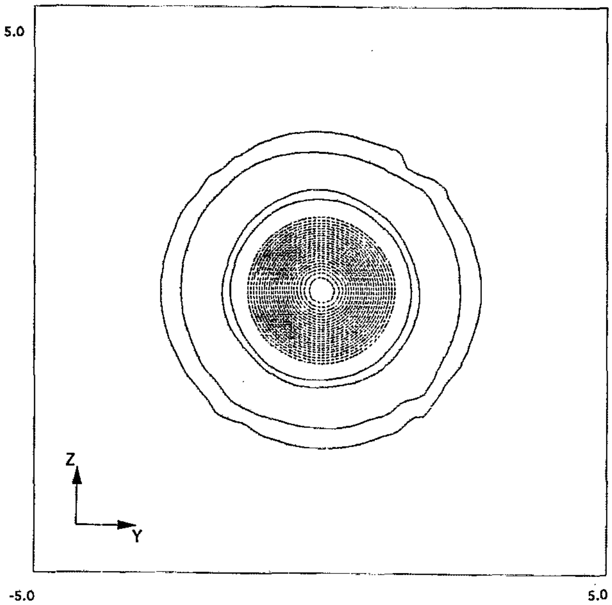

FIG. 5. Axial vorticity contours in a cross (YZ) plane for the Taylor vortex. Time$=6(\delta_0/U_0)$, $\omega_{\max}=3.25$, $\omega_{\min}=-0.46$. The dashed lines indicate regions of positive vorticity. Initially the core consists of positive vorticity and the outer regions consist of negative vorticity.

First, the cross-sectional structure of the vortex core at a certain axial location is shown for the Taylor vortex. For plotting purposes a smaller domain is shown. The contours of axial vorticity at three different times in a plane normal to the axial direction are shown in Figs. 5–7. The solid lines indicate negative vorticity contours. Early in the simulation, at $T=6$, the core consists of positive vorticity surrounded by negative vorticity in the outer region, as shown in Fig. 5. Initially, new structures develop outside the core region. The contours at $T=15$, shown in Fig. 6, show new developments in the region outside the core. But the core is well organized at this instant. Later, these structures that are formed outside the core interact with the core, resulting in the generation of small-scale motions inside the core. The axial vorticity contours at $T=27$ shown in Fig. 7 confirm this conclusion. Both positive and negative vorticity contours are seen embedded within each other, which is a sign of small-scale motions in these regions.

Next, we look at the evolution of the axial vorticity contours in the meridional (XY) plane. Figure 8 shows the contours at an early time of $T=6$. The core and the outer region are well organized. Later, at $T=15$, new structures appear outside the core, while the region very close to the core retains its initial vorticity distribution, as shown in Fig. 9. In Fig. 10 is shown the contours at $T=27$. The new struc-

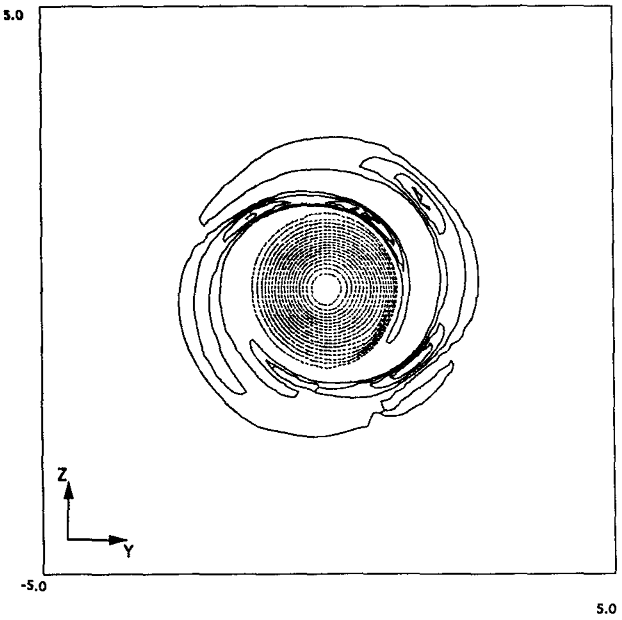

FIG. 6. Axial vorticity contours in a cross (YZ) plane for the Taylor vortex. Time=15(δ_0/U_0), $\omega_{\max}=3.21$, $\omega_{\min}=-0.97$. The core region remains almost intact, while the outer region has developed new structures.

tures that appear in the region outside the core later move into the core, destroying its initial organization.

Three-dimensional isovorticity plots are shown next. Isosurfaces of the magnitudes of the axial and the azimuthal vorticity components at two different times are shown in Figs. 11 and 12 for the Taylor vortex. The three-dimensional (3-D) view gives a clearer picture of the large-scale structures that are being generated. The surfaces shown correspond to a high value of the streamwise and azimuthal com-

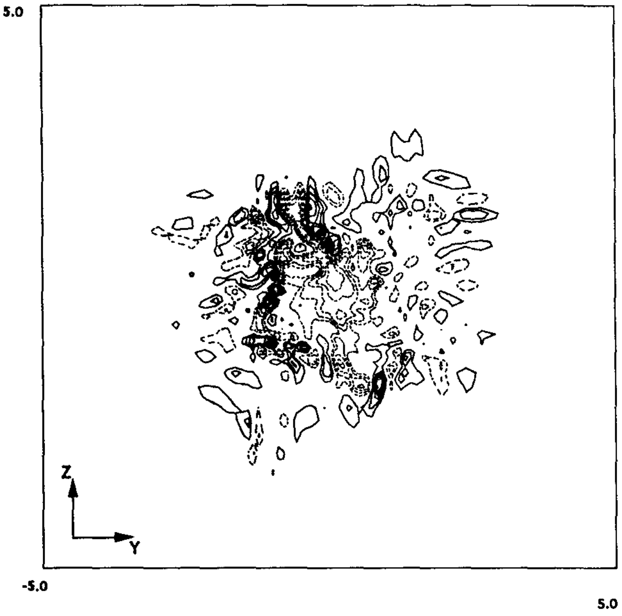

FIG. 7. Axial vorticity contours in a cross (YZ) plane for the Taylor vortex. Time=27(δ_0/U_0), $\omega_{\max}=5.70$, $\omega_{\min}=-5.60$. The structures from the outer region has penetrated the core at this time.

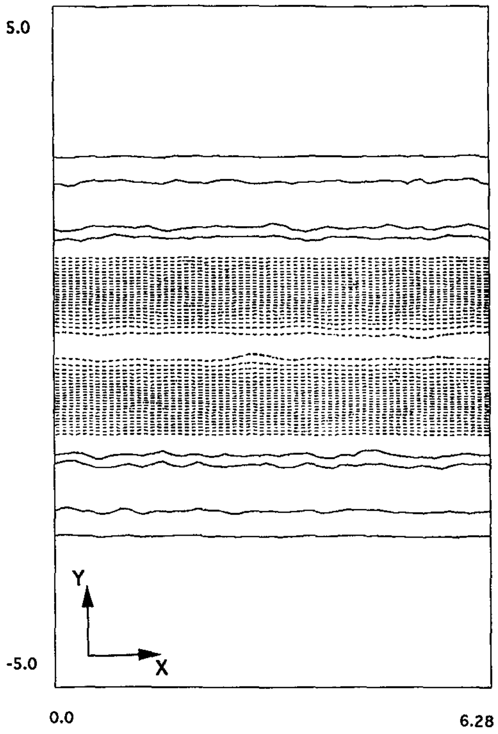

FIG. 8. Axial vorticity contours in a meridional (XY) plane for the Taylor vortex. Time=6(δ_0/U_0), $\omega_{\max}=3.30$, $\omega_{\min}=-0.47$. The dashed lines indicate positive vorticity. The core region is well organized at this time.

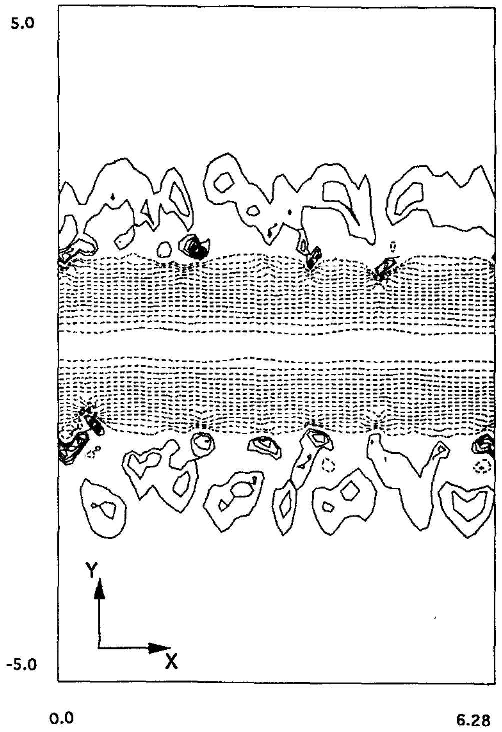

FIG. 9. Axial vorticity contours in a meridional (XY) plane for the Taylor vortex. Time=15(δ_0/U_0), $\omega_{\max}=3.32$, $\omega_{\min}=-1.47$. New structures are seen in the outer regions, while the core remains intact.

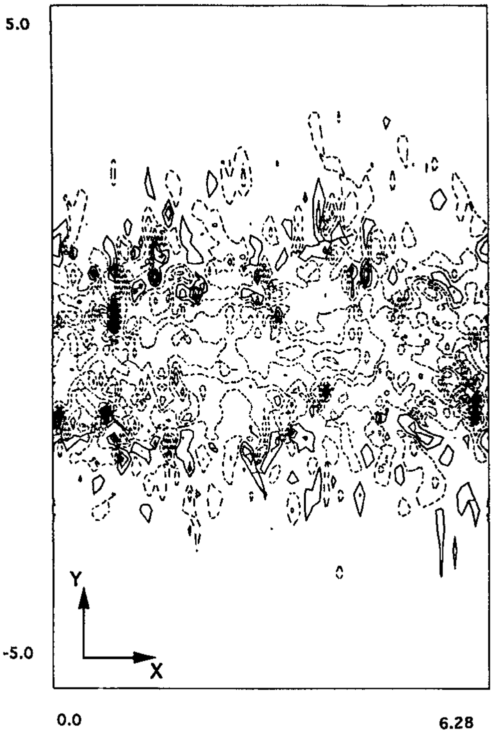

FIG. 10. Axial vorticity contours in a meridional (XY) plane for the Taylor vortex. Time$=27(\delta_0/U_0)$, $\omega_{\max}=6.97$, $\omega_{\min}=-11.45$. The core and the outer regions are indistinguishable.

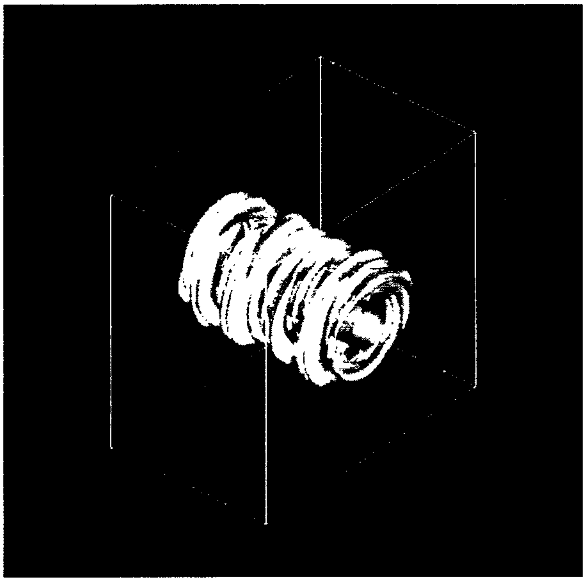

FIG. 11. Isovorticity surfaces for the Taylor vortex. Time$=15(\delta_0/U_0)$, $\omega_x=1.6$, $\omega_\theta=0.80$. The surface of constant streamwise vorticity is a cylindrical surface and the surface of constant azimuthal vorticity is in the shape of incomplete rings around the cylinder.

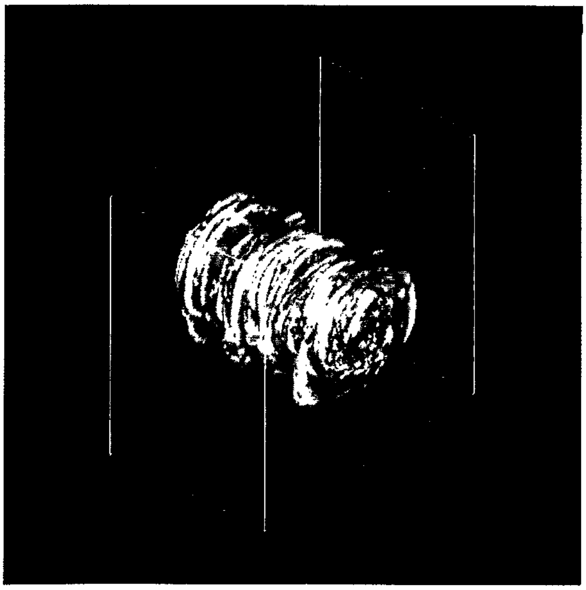

FIG. 12. Isovorticity surfaces for the Taylor vortex. Time$=19(\delta_0/U_0)$, $\omega_x=2.0$, $\omega_\theta=1.90$. The surface of constant streamwise vorticity is not completely visible.

ponents of the vorticity present in the flow field at that instant. Initially, streamwise vorticity is concentrated in the core, and only the core is visible at high vorticity levels. Due to instabilities, vortical structures develop outside the core. These structures gradually envelop the core completely, as seen from the isovorticity surfaces at $T=15$ given in Fig. 11. The ring-shaped structures seen encircling the core are surfaces of high azimuthal vorticity. We recall that the azimuthal vorticity in the computational domain during the early stages of the simulation was negligible compared to the streamwise vorticity in the core. Later, these structures interact with the core, resulting in the destruction of the organized nature of the core. The isovorticity surfaces at $T=19$, shown in Fig. 12, confirm this conclusion. As we continue the simulation, no more large structures are generated. The structures that are initially formed around the core are similar to the donut-shaped rings seen in a Taylor–Couette flow between two cylinders. These are created in the region of decreasing circulation due to the Rayleigh–Taylor centrifugal instability. These ring-shaped structures are counter-rotating vortices. The velocity vectors in the meridional (XY) plane shown in Fig. 13 confirm that these structures are indeed counter-rotating vortices. Similar structures were seen by Melander and Hussain[55] in their direct numerical simulations. The U-shaped vortices observed around a vortex core close to a solid wall or a free surface by Dommermuth[25] are also similar to these structures.

The Oseen vortex, on the other hand, is linearly stable. No new structures are seen for the Oseen vortex. Figure 14 shows the axial vorticity contours in a cross-plane (YZ) at $T=51$. The contours look very organized, and there are no signs of the formation of new structures, even at this late stage in the simulation.

E. Turbulent kinetic energy

The evolution of turbulent kinetic energy for both of the vortices is compared in Fig. 15. The turbulent kinetic energy is obtained by taking the average of

$$E=\tfrac{1}{2}(u'^2+v'^2+w'^2)$$

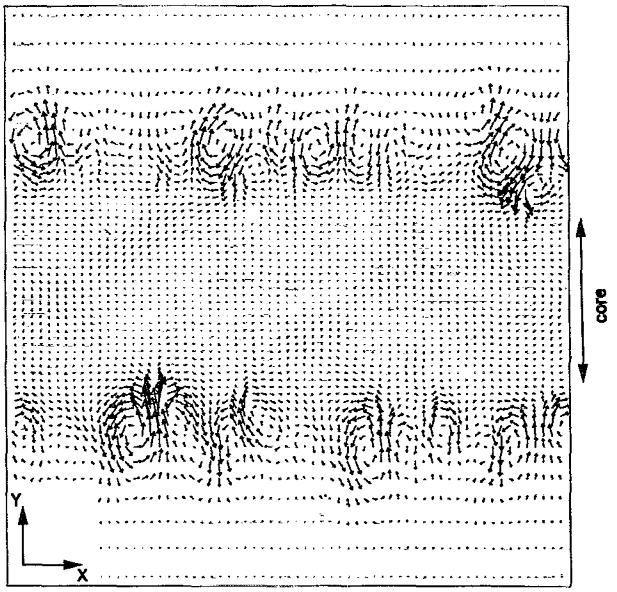

FIG. 13. Velocity vectors in the meridional (XY) plane for the Taylor vortex. Time=15(δ_0/U_0). Counter-rotating vortices are seen on both edges of the vortex core. The initial core is also marked.

in the axial direction and then integrating in the r-θ plane. Here

$$u'(r,\theta,x,t)=\tilde{u}(r,\theta,x,t)-\tilde{\mathbf{U}}(r,t),$$

with similar expressions for v' and w'. Here $\tilde{\mathbf{U}}$ is the instantaneous tangential profile averaged in the axial and the azimuthal directions.

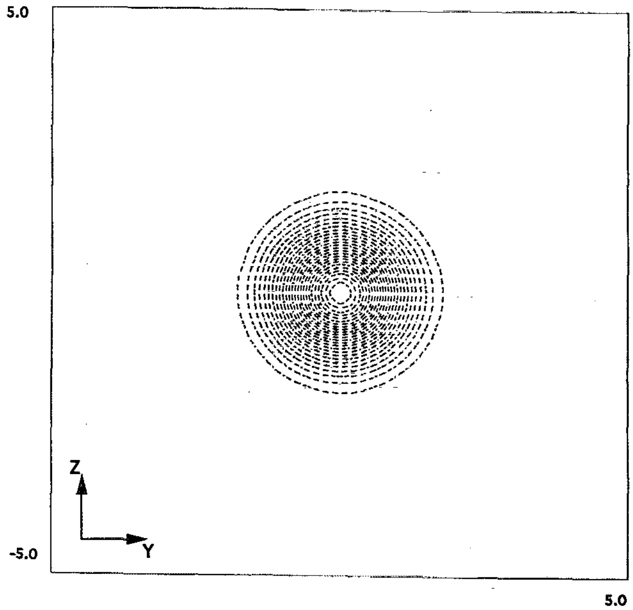

FIG. 14. Axial vorticity contours in a cross (YZ) plane for the Oseen vortex. Time=51(δ_0/U_0), $\omega_{\max}$=3.26, $\omega_{\min}$=0.00. No significant structures are visible.

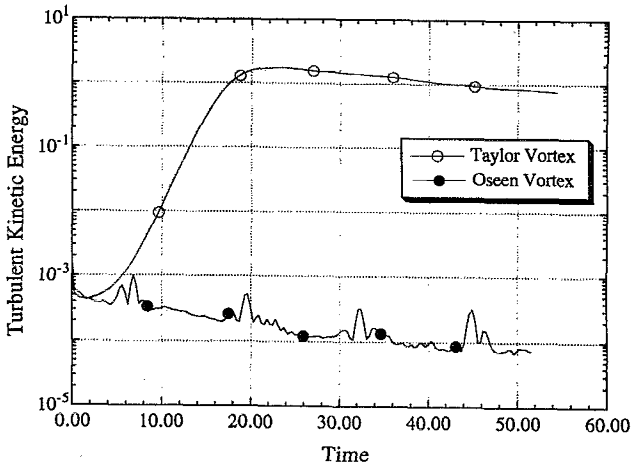

FIG. 15. Evolution of turbulent kinetic energy for the Taylor vortex and the Oseen vortex. Same random initial conditions were used for both the simulations. While the Taylor vortex went through a transition process after an initial reorganization, the Oseen vortex showed no tendency to amplify the disturbances.

The turbulent kinetic energy in the Taylor vortex decreases for a short period of time and then increases. The initial decrease in kinetic energy is attributed to the reorganization of the flow field, due to the unphysical nature of the initial random perturbations. Once the flow adjusts itself, various modes start to grow. This explains the rapid growth of kinetic energy. The creation of the structures around the core is an indication of the growth of the modal energies. The breakdown of these structures into small-scale motions represents the generation of turbulence. The turbulent kinetic energy then saturates at a nondimensional time of about 24 (the time taken by a particle with the maximum tangential velocity to encircle the core four times approximately), and then a period of slow decay sets in. The Oseen vortex, on the other hand, shows no significant turbulence growth. The modal energies also show no growth. For the Taylor vortex many modes are active and growing, while for the Oseen vortex none of the modes are growing.

Figure 16 shows the growth of the (2,0) mode for the Taylor vortex. The solid line indicates the linear stability predicted curve and the open circles the numerical simulation. After the initial flow reorganization, the mode is growing according to the linear stability. Recall that the initial disturbances were random.

F. Mean velocity profile

Figure 17 shows the decay of the mean tangential velocity profile for the Taylor vortex. The mean profile shows no significant decay, up to a nondimensional time of about 20. Then it starts to decay quite rapidly. The initial persistence of the mean profile is attributed to the absence of turbulent stresses. The most significant component of turbulent stresses is found to be $\overline{u_r'u_\theta'}$; where the overbar means averaging in the axial direction. The distribution of this component along a line through the vortex center is shown in Fig. 18 at three different times. The low level of $\overline{u_r'u_\theta'}$ is clear at early times. Since this simulation is for a high Reynolds number, viscous effects are negligible. As the large-scale structures appear, the effect of turbulent stresses becomes significant. The large-scale structures are the mechanism by

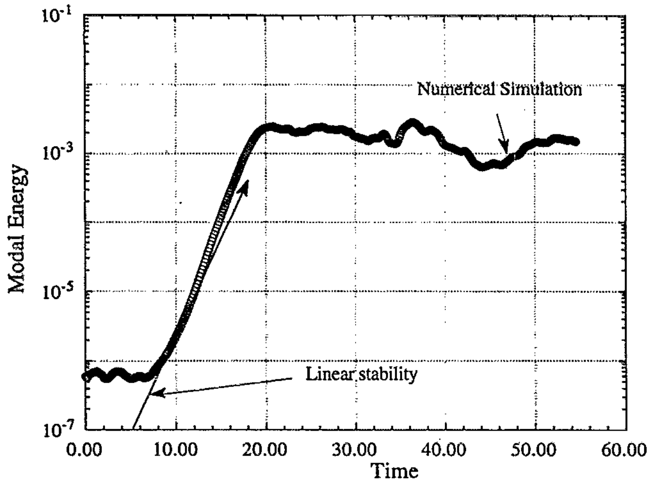

FIG. 16. Evolution of modal kinetic energy of the (2,0) mode for the Taylor vortex. Even though the initial perturbations were random, the axisymmetric mode is growing according to the linear theory after a period of initial reorganization.

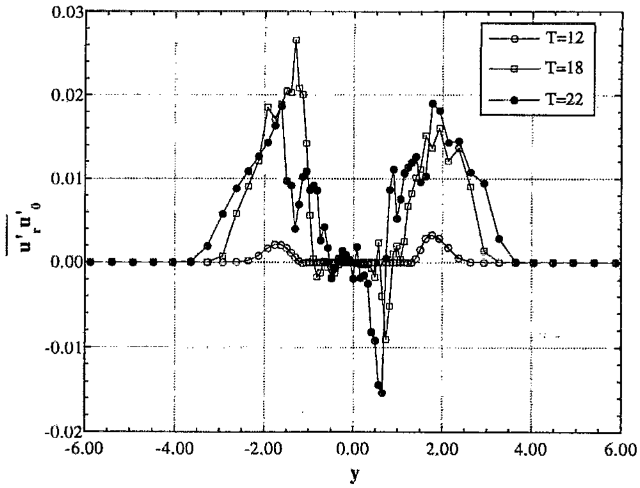

FIG. 18. Distribution of $\overline{u'_r u'_\theta}$ along a line through the center of the vortex at different times. Early in the simulation, $\overline{u'_r u'_\theta}$ is negligible.

which angular momentum is exchanged between the core and the relatively stagnant surroundings. The rapid decay of the mean tangential velocity is attributed to this transfer of angular momentum. Although the core radius decreases initially, it starts to increase as the flow becomes turbulent. The mean tangential velocity profile of the Oseen vortex, on the other hand, shows no significant decay, as shown in Fig. 19. This is because of the absence of large-scale instabilities.

Since the Oseen vortex does not indicate transition to turbulence, attention is now focused on the Taylor vortex, and all the following observations are for the Taylor vortex only. In Fig. 20, the normalized circulation at a nondimensional time of 24 is compared with the universal inner region described by Hoffman and Joubert.[11] The inner power region and the logarithmic regions are clearly distinguishable. To better see the logarithmic region, we plotted the function $C=(\Gamma/\Gamma_1-1)/\ln(r/r_1)$ in Fig. 21. Here Γ_1 and r_1 are the circulation and radius at the point of maximum tangential velocity, respectively. This function should be exactly 1 in the logarithmic region. At $T=0$, clearly there is no logarithmic region. Later in time, we can see a logarithmic region near the core radius. The logarithmic region extends from 0.7 to 1.2 approximately. Saffman,[15] in his analysis, places the logarithmic region between 0.8 and 1.2. The experiments of Hoffman and Joubert[11] were, for turbulent vortices, with a monotone variation of circulation. But the calculations here are for a Taylor vortex, which initially had a nonmonotone variation of circulation. To clear this point, we plotted the normalized circulation profiles for the Taylor vortex at different times, as shown in Fig. 22. We note that as the vortex became turbulent, the circulation profile became flatter away from the core, which is typical of the trailing vortices used in the experiments of Hoffman and Joubert.[11] This explains the good comparison shown in Fig. 20.

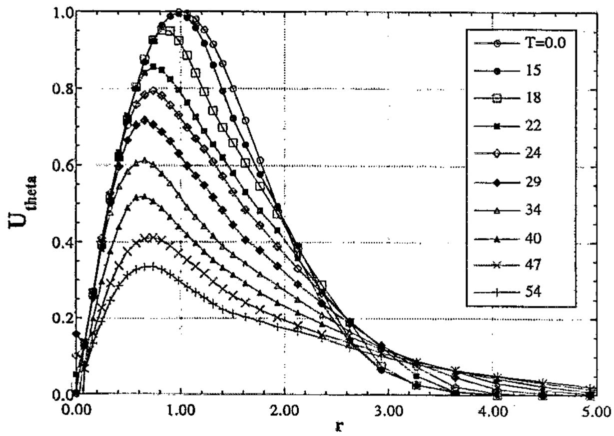

FIG. 17. Decay of the mean velocity profile for the Taylor vortex. The mean flow shows no significant decay up to a time of about 20 due to the absence of turbulent stresses and low molecular viscosity (Re=100 000). Later as the vortex became turbulent the mean flow shows rapid decay.

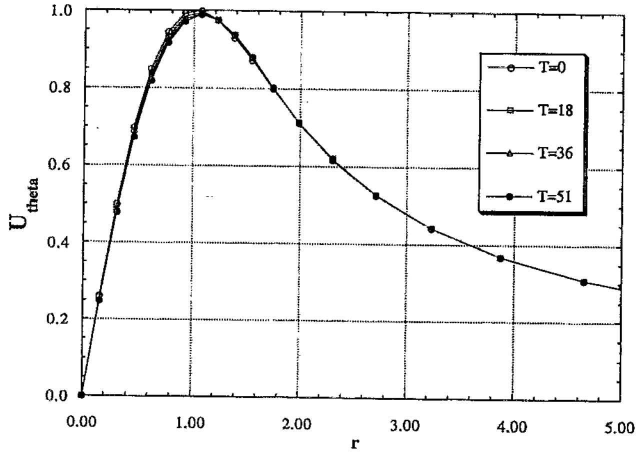

FIG. 19. Evolution of the mean velocity profile for the Oseen vortex. The mean flow shows no significant decay due to low molecular viscosity (Re =100 000) and the absence of any instability mechanisms.

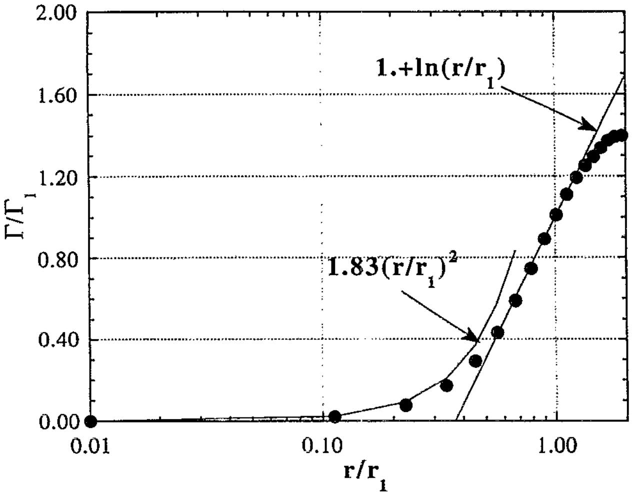

FIG. 20. Comparison of normalized mean circulation profile with the experimental profile of Hoffman and Joubert for the Taylor vortex. The circles denote the present numerical simulation. The inner power region and the log region are visible. Time$=25(\delta_0/U_0)$.

Since these computations were done using the dynamic model, the model constant C_R was obtained as a function of time, and the spatial directions in the cross-plane. Figure 23 shows the value of C_R integrated over the cross-plane as a function of time. Although this integrated value does not have any physical significance, it, nevertheless, gives a general idea about the relative magnitude of C_R as the vortex changes from a laminar vortex to a turbulent vortex. The integrated value shows a steady growth during the transition period before it leveled off. This behavior is a reflection of the ability of the dynamic model to vary according to the state of the flow field.

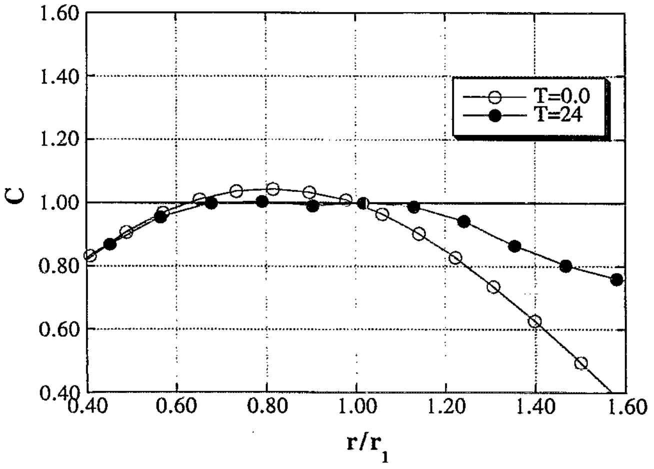

FIG. 21. Comparison of C in the empirical formula of Hoffman and Joubert. Here $C=(\Gamma/\Gamma_1-1)/\ln(r/r_1)$, should be exactly 1.0 in the logarithmic region. The logarithmic region extends from 0.7 to 1.2 approximately. Note that the initial profile has no logarithmic region.

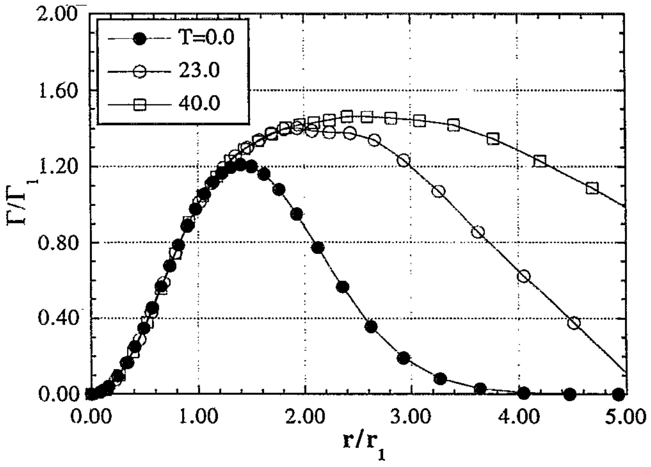

FIG. 22. Normalized mean circulation profiles at different times for the Taylor vortex. The normalized circulation profile has become flatter as the flow became turbulent.

IV. CONCLUSIONS

Large-eddy simulation is used to study the growth and breakdown of large-scale structures in stationary longitudinal vortices due to centrifugal instabilities. The dynamic subgrid-scale model is used to model the subgrid-scale stress tensor.

New large-scale structures around the core of the Taylor vortex have been observed. In this vortex the circulation is a nonmonotone function of radius. The mechanism of generating these structures is the Rayleigh centrifugal instability. These structures appear as counter-rotating vortex rings around the vortex core similar to the donut-shaped structures found in a Taylor–Couette flow. These structures are generated by the vortex flow field from random disturbances superimposed on the mean profile. These rings gradually envelop the vortex core completely. Eventually, both the core and the rings become indistinguishable, as chaos prevails.

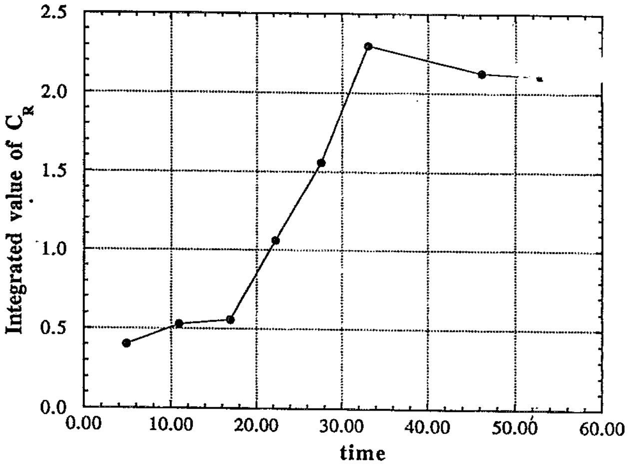

FIG. 23. Integrated value of C_R as a function of time. This curve reflects the relative magnitude of C_R with time.

Associated with the breaking of the core, the turbulent kinetic energy in the vortex reaches a maximum. Subsequently, the turbulent kinetic energy decays because no new large-scale structures are produced as the mechanism of generating the large-scale structures is weakened.

Initially, the turbulent kinetic energy showed strong growth during the transition process, until the vortex became fully turbulent. Then it leveled off, and a period of slow decay followed. The modal kinetic energy after the initial reorganization showed the same growth rate, as predicted by the linear stability theory.

The mean velocity profile showed no decay during the initial stages. Once the turbulent kinetic energy attained the maximum level signalling the end of transition, the mean flow started to decay rapidly.

The normalized circulation profile showed good agreement with the universal inner region of Hoffman and Joubert[11] once the flow became fully turbulent. The inner region consists of a power region and a logarithmic region.

The Oseen vortex has a monotone radial distribution of circulation; the Rayleigh instability mechanism is absent. No large-scale structures were generated. The mean profile showed no signs of decay while the kinetic energy of the initial random disturbance showed a very slow decay.

The dynamic subgrid-scale model correctly modeled the transition period. Initially the model predicted very low values for the model constant. During the transition period the value of the constant grew rapidly until saturation, and then it leveled off.

ACKNOWLEDGMENT

This work is supported by the Office of Naval Research under Grant No. N00014-92-J-4087.

[1] Lord Rayleigh, "On the dynamics of revolving fluids," Proc. R. Soc. London Ser. A **93**, 148 (1916).

[2] M. Germano, U. Piomelli, P. Moin, and W. Cabot, "A dynamic subgrid-scale eddy-viscosity model," Phys. Fluids A **3**, 1760 (1991).

[3] P. Moin, K. Squire, W. Cabot, and S. Lee, "A dynamic subgrid-scale model for compressible turbulence and scalar transport," Phys. Fluids A **3**, 2746 (1991).

[4] D. K. Lilly, "A proposed modification of the Germano subgrid-scale closure method," Phys. Fluids A **3**, 633 (1992).

[5] V. C. Wong, "A proposed statistical-dynamic closure method for the linear or nonlinear subgrid-scale stresses," Phys. Fluids A **4**, 1080 (1992).

[6] H. Lamb, *Hydrodynamics* (Dover, New York, 1945).

[7] H. B. Squire, "The growth of a vortex in turbulent flow," Aerosp. Q. **8**, 302 (1965).

[8] B. G. Newman, "Flow in a viscous trailing vortex," Aerosp. Q. **10**, 149 (1959).

[9] D. S. Dosanjh, E. P. Gasparek, and S. Eskinazi, "The decay of a viscous trailing vortex," Aerosp. Q. **13**, 167 (1962).

[10] P. R. Owen, "The decay of a turbulent trailing vortex," Aerosp. **2**, 69 (1970).

[11] E. R. Hoffman and P. N. Joubert, "Turbulent line vortices," J. Fluid Mech. **16**, 395 (1963).

[12] J. N. Nielsen and R. G. Schwind, "Decay of a vortex pair behind an aircraft," *Aircraft Wake Turbulence and Its Detection* (Plenum, New York, 1971), pp. 413–454.

[13] S. P. Govindaraju and P. G. Saffman, "Flow in a turbulent trailing vortex," Phys. Fluids A **14**, 2074 (1991).

[14] M. S. Uberoi, "Mechanisms of decay of laminar and turbulent vortices," J. Fluid Mech. **90**, 241 (1979).

[15] P. G. Saffman, "Structure of turbulent line vortices," Phys. Fluids **16**, 1181 (1973).

[16] W. R. C. Phillips, "The turbulent trailing vortex during roll-up," J. Fluid Mech. **105**, 451 (1981).

[17] B. W. McCormick, J. L. Tangler, and H. E. Sherrierb, "Structure of trailing vortices," J. Aircr. **5**, 260 (1968).

[18] N. A. Chigier and V. R. Corsiglia, "Wind-tunnel studies of wing wake turbulence," J. Aircr. **9**, 820 (1972).

[19] V. R. Corsiglia, R. G. Schwind, and N. A. Chigier, "Rapid scanning, three-dimensional hot-wire anemometer surveys of wing-tip vortices," J. Aircr. **10**, 752 (1973).

[20] D. K. Lezius, "Water tank study of the decay of trailing vortices," AIAA J. **12**, 1065 (1974).

[21] T. Sarpkaya, and P. Suthon, "Scarred and striated signature of a vortex pair on the free surface," Proceedings of the 18th Symposium on Naval Hydrodynamics, 1990, pp. 503–520.

[22] T. Sarpkaya and P. Suthon, "Interaction of a vortex couple with a free surface," Exp. Fluids **11**, 205 (1991).

[23] T. Sarpkaya, "Three dimensional interactions of vortices with a free surface," AIAA Paper No. 92-0059, 1992.

[24] D. G. Dommermuth and D. K. P. Yue, "A numerical study of three dimensional viscous interactions of vortices with a free surface," in Ref. 21, pp. 727–788.

[25] D. G. Dommermuth, "The formation of U-shaped vortices on vortex tubes impinging on a wall with applications to free surfaces," Phys. Fluids A **4**, 757 (1992).

[26] C. P. Donaldson and R. D. Sullivan, "Decay of an isolated vortex," *Aircraft Wake Turbulence and Its Detection* (Plenum, New York, 1971), pp. 389–411.

[27] E. D. Poppleton, "Preliminary experimental investigation of the structure of a turbulent trailing vortex," Report TN 71-1, Mechanical Engineering Research Laboratories, McGill University, Montreal, P.Q., Canada, March, 1971.

[28] P. I. Singh, Doctoral dissertation, University of Colorado, Boulder, CO, 1974.

[29] W. R. C. Phillips and J. A. H. Graham, "Reynolds-stress measurements in a turbulent trailing vortex," J. Fluid Mech. **147**, 353 (1984).

[30] S. I. Green and A. J. Acosta, "Unsteady flow in trailing vortices," J. Fluid Mech. **227**, 107 (1991).

[31] R. A. Giranger, "Turbulent vortices," in *Introduction to Vortex Dynamics*, Von Kármán Lecture Series, 26–30 May 1986 (Von Kármán Institute for Fluid Dynamics, Rhode Saint Genèse, Belgium, 1986), Vol. 1, pp. 1986–2008.

[32] D. G. Lilley, "Prediction of inert turbulent swirl flows," AIAA J. **11**, 955 (1973).

[33] B. S. Baldwin, N. A. Chigier, and Y. S. Sheaffer, "Prediction of far flow field in trailing vortices," AIAA Paper No. 72-989, 1972.

[34] A. J. Bilanin, M. E. Teske, and J. E. Hirsch, "Neutral atmospheric effects on the dissipation of aircraft vortex wakes." AIAA J. **16**, 956 (1978).

[35] Z. Zheng and R. L. Ash, "Prediction of turbulent wake vortex motion near the ground," *Transitional and Turbulent Compressible Flows*, ASME Fluid Dynamics Conference (ASME, New York, 1993), Vol. 151, pp. 195–207.

[36] S. Hogg and M. A. Leschziner, "Computation of highly swirling confined flow with a Reynolds stress turbulence model," AIAA J. **27**, 57 (1989).

[37] D. G. Sloan, P. J. Smith, and L. D. Smoot, "A second order modeling study of confined swirling flow," Prog. Energy Combust. Sci. **12**, 163 (1986).

[38] J. M. Khodadadi and N. S. Vlachos, "Effects of turbulence model constants on computation of confined swirling flows," AIAA. J. **28**, 750 (1990).

[39] M. Nikjooy and H. C. Mongia, "A second order modeling study of confined swirling flow," Int. J. Heat Fluid Flow **12**, 12 (1991).

[40] K. H. Chang, and C. S. Chen, "Development of a hybrid $k-\epsilon$ turbulence model for swirling recirculating flows under moderate to strong swirl intensities," Int. J. Num. Methods Fluids **16**, 421 (1993).

[41] J. Smagorinsky, "General circulation experiments with the primitive equations. I. The basic experiment," Mon. Weather Rev. **91**, 99 (1963).

[42] J. Bardina, J. H. Ferziger, and R. S. Rogallo, "Effects of rotation on isotropic turbulence: computation and modeling," J. Fluid Mech **154**, 321 (1985).

[43] K. D. Squire, "Large eddy simulation of rotating isotropic turbulence," *Engineering Applications of LES*, ASME Fluid Dynamics Conference, 1993 (ASME, New York, 1993), Vol. 62, pp. 65–72.

[44] G. Erlebacher, M. Y. Hussaini, C. G. Speziale, and T. A. Zang, "Toward

the large-eddy simulation of compressible turbulent flows," J. Fluid. Mech. **238**, 155 (1992).

[45] S. A. Ragab, S. Sheen, and M. K. Sreedhar, "An investigation of finite-difference methods for large-eddy simulation of a mixing layer," AIAA Paper No. 92-554, 1992.

[46] T. A. Zang, R. B. Dahlburg, and J. P. Dahlburg, "Direct and large-eddy simulations of three-dimensional compressible Navier–Stokes turbulence," Phys. Fluids A **4**, 127 (1992).

[47] N. M. El-Hady, T. A. Zang, and U. Piomelli, "Dynamic subgrid-scale modeling for high-speed transitional boundary layers," *Engineering Applications of LES*, ASME Fluid Dynamics Conference (ASME, New York, 1993), Vol. 162, pp. 103–110.

[48] J. Liu and U. Piomelli, "Interaction of embedded streamwise vortices with a spatially developing boundary layer," in Ref. 47, pp. 45-53.

[49] K. Akselvoll and P. Moin, "Application of the dynamic localization model to LES of turbulent flow over a backward facing step," in Ref. 47, pp. 1–6.

[50] Y. Zang, R. L. Street, and J. R. Koseff, "Large simulation of turbulent cavity flow using a dynamic SGS model," in Ref. 47, pp. 121–127.

[51] M. K. Sreedhar, Doctoral dissertation, Virginia Polytechnic Institute and State University, Blacksburg, VA, 1994.

[52] D. Gottlieb and E. Turkel, "Dissipative two–four methods for time-dependent problems," Math. Comput. **30**, 703 (1976).

[53] R. Panton, *Incompressible Flow* (Wiley, New York, 1984).

[54] M. R. Lessen, P. J. Singh, and F. Paillet, "The stability of a trailing line vortex. Inviscid theory," J. Fluid Mech. **65**, 753 (1974).

[55] V. M. Melander and F. Hussain, "Polarized vorticity dynamics on a vortex column," Phys. Fluids A **5**, 1992 (1993).